Astronomy & Astrophysics manuscript no. paperII
October 26, 2022

Transverse oscillations in 3D along Ca II K bright fibrils in the Solar chromosphere

Sepideh Kianfar[1], Jorrit Leenaarts[1], Sara Esteban Pozuelo[1,2,3], João M. da Silva Santos[4], Jaime de la Cruz Rodríguez[1], and Sanja Danilovic[1]

[1] Institute for Solar Physics, Dept. of Astronomy, Stockholm University, Albanova University Center, 10691 Stockholm, Sweden
[2] Instituto de Astrofísica de Canarias, C/Vía Láctea s/n, E-38205 La Laguna, Tenerife, Spain
[3] Universidad de La Laguna, Dept. Astrofísica. E-38206 La Laguna, Tenerife, Spain
[4] National Solar Observatory, 3665 Discovery Drive, Boulder, CO 80303, USA

Received Month dd, yyyy; accepted Month dd, yyyy

ABSTRACT

Context. Fibrils in the solar chromosphere carry transverse oscillations as determined from non-spectroscopic imaging data. They are estimated to carry an energy flux of several kW m^{-2}, which is a significant fraction of the average chromospheric radiative energy losses.
Aims. We aim to determine oscillation properties of fibrils not only in the plane-of-the-sky (horizontal) direction, but also along the line-of-sight (vertical) direction.
Methods. We obtained imaging-spectroscopy data in Fe I 6173 Å, Ca II 8542 Å, and Ca II K obtained with the Swedish 1-m Solar Telescope. We created a sample of 120 bright Ca II K fibrils and measured their horizontal motions. Their vertical motion was determined through non-LTE inversion of the observed spectra. We determined the periods and velocity amplitudes of the fibril oscillations, as well as phase differences between vertical and horizontal oscillations in the fibrils.
Results. The bright Ca II K fibrils carry transverse waves with a mean period of 2.2×10^2 s, and a horizontal velocity amplitude of 2 km s^{-1}, consistent with earlier results. The mean vertical velocity amplitude is 1 km s^{-1}. We find that 118 out of the 120 fibrils carry waves in both the vertical and horizontal directions, and 55 of those have identical periods. For those 55, we find that all phase differences between 0 and 2π occur, with a mild but significant preference for linearly polarized waves (phase difference of 0 or π).
Conclusions. The results are consistent with the scenario where transverse waves are excited by granular buffeting at the photospheric footpoints of the fibrils. Estimates of transverse wave flux based on imaging data only are too low because they ignore the contribution of the vertical velocity.

Key words. Sun: atmosphere – Sun: chromosphere – Sun: oscillations – Methods: observational

1. Introduction

The solar chromosphere is pervaded by waves and oscillations that are excited by the convection and p-modes in the photosphere (e.g., Jess et al. 2015, and references therein). These waves are considered a prime candidate to transport the energy needed to sustain chromospheric radiative losses from the photosphere into the chromosphere.

In areas where the gas pressure is stronger than the magnetic pressure (plasma $\beta > 1$) acoustic-gravity waves dominate. They are well-understood, both observationally and theoretically (e.g. Carlsson & Stein 1997; Wedemeyer et al. 2004), but the size of their contribution to the required energy input remains under debate (Carlsson et al. 2019). In areas where the magnetic pressure is stronger ($\beta < 1$), the situation is more complex. In a homogeneous plasma there are now three waves, the slow and fast magneto-acoustic wave and the Alfvén wave. The chromosphere is obviously not homogeneous, and a large literature exists about waves in homogenous magnetic cylinders (referred to as flux tubes in the literature) with the field aligned to the axis of the cylinder, taken as an approximation of magnetic field bundles (e.g. Edwin & Roberts 1983; Zaqarashvili & Erdélyi 2009; Goossens et al. 2009). In this geometry there is a complex set of wave modes, including torsional waves, oscillations of the tube diameter (sausage modes), and a swaying of the whole tube (kink modes). The most frequently identified observationally is the kink mode, as it manifests itself as clearly swaying structures in imagery, especially of spicules that protrude above the limb of the Sun (e.g. De Pontieu et al. 2007; Suematsu et al. 2008).

Propagating transverse oscillations of fibrils and mottles, elongated chromospheric structures that emanate from photospheric magnetic elements, have been observed using imaging data in chromospheric spectral lines, e.g., Pietarila et al. (2011); Kuridze et al. (2012); Morton et al. (2014); Jafarzadeh et al. (2017a). These oscillations have typically been interpreted as kink waves. Observed velocity amplitudes are on the order of 5 km s^{-1}, periods in the range of 16 – 600 s, and phase speeds of 50 – 300 km s^{-1}. Shetye et al. (2021) studied high frequency waves in spicule-like event using imaging spectroscopy on Hα. In addition to plane-of-the-sky (POS) velocities, they use Doppler shift information to estimate line of sight (LOS) velocity of the spicules. They find periods in the range of 40 – 200 s, and velocity amplitudes around 5–20 km s^{-1}.

However, when radial and longitudinal inhomogeneities are introduced in magnetic concentrations, the separation between the different wave types becomes more difficult (Srivastava et al.

Send offprint requests to: Sepideh Kianfar e-mail: sepideh.kianfar@astro.su.se

2021). Radiation-MHD models of the chromosphere show proxies of different wave types often appear in the same location and become indistinguishable (Danilovic 2022).

Leenaarts et al. (2015) investigated the relation between oscillations as seen in Hα imagery and transverse oscillations propagating along magnetic field lines in a radiation-MHD simulation of network. They warned that observed fibrils might not always trace out single field lines, so that interpretation of observations in terms of kink waves along flux tubes must be done with caution. However, radiative transfer computations by Bjørgen et al. (2019) based on a radiation-MHD simulation of an active region, indicate that strong fibrils seen in Hα, Mg II k, and Ca II K trace field lines to a much larger degree than in the network simulations.

Several observations of transverse oscillations in off-limb spicules using both POS swaying and LOS motions through measuring Doppler shifts of line profiles exist (e.g., Gadzhiev & Nikolskii 1982; De Pontieu et al. 2012; Antolin et al. 2018) ,but only one where on-limb fibrils are considered (Shetye et al. 2021). In the latter study, Doppler shifts in Hα are used to trace the LOS variations in velocity which significantly limits the accuracy.

In this paper we exploit imaging spectroscopy data obtained at the Swedish 1-m Solar telescope in multiple spectral lines combined with non-LTE inversion to trace the LOS components of transverse oscillations. This ensures that the LOS velocity is better resolved. We focus on oscillations in fibrils that appear bright in Ca II H&K data (Jafarzadeh et al. 2017a; Kianfar et al. 2020). The physical properties of these bright fibrils have been studied by Kianfar et al. (2020). We report here on both POS and LOS velocity and displacement amplitudes, wave periods, and correlations between the POS and LOS properties.

2. Observations

2.1. Data preparation

We analyse observations of a fibrillar area centered at $(X, Y) = [70\farcs4, 153\farcs2]$, i.e. $\mu = 0.98$, taken at the Swedish 1-m Solar Telescope (SST; Scharmer et al. 2003). The observed field of view (FoV) was located at the edge of a plage region in the AR12716. The observations were acquired on 2018-07-22, from 08:23:58 to 08:53:25 UT using the CRisp Imaging Spectro-Polarimeter (CRISP; Scharmer et al. 2008) and CHROMospheric Imaging Spectrometer (CHROMIS Scharmer 2017) instruments. Seeing conditions were excellent throughout the whole observing time.

The Fe I 6173 Å line was sampled by CRISP in 13 equidistant wavelength positions in a range of ±180 mÅ around the line centre. CRISP also observed the Ca II 8542 Å line. It was sampled at 21 equidistant wavelength positions between ±550 mÅ as well as two extra points at ±880 Å from the line core. Both lines were observed with full Stokes polarimetry and with a total cadence of 21 s.

CHROMIS observed the Ca II K line in 27 equidistant wavelength positions in the range ±1.5 Å around the line core. In addition, it observed an additional wavelength point at 4000 Å (continuum). The CHROMIS observations have a cadence of 8 s.

The observed data were reconstructed by applying the CRISPRED reduction pipeline (de la Cruz Rodríguez et al. 2015) to the CRISP data and SSTRED (Löfdahl et al. 2021) to the CHROMIS observations. The image restoration used in the reconstruction pipelines is the Multi-Object Multi-Frame Blind Deconvolution (MOMFBD; van Noort et al. 2005) method. After reconstruction, the CRISP and CHROMIS images were co-aligned with an accuracy of about 0.1 pixel. The CRISP data were resampled from a pixel size of $0\farcs059$ to the CHROMIS pixel size of $0\farcs038$. It was also resampled in time to the CHROMIS cadence using nearest-neighbour interpolation. The data were calibrated to the absolute intensity by comparing the average intensity profile in a quiet region in the field of view to a solar atlas profile (Neckel & Labs 1984).

2.2. Overview of the FoV

Figure 1 and the accompanying animation show an overview of the observations. The upper-left corner of the FoV contains a plage region with a concentration of unipolar small-scale magnetic features as seen in the linear and circular polarization maps (Fig. 1c and 1d). The area surrounding the plage region is covered with a forest of elongated bright fibrils in the chromosphere (Fig. 1b). The Ca II 8542 Å line core image in Fig. 1e shows a fibrillar pattern similar to the one in Ca II K (cf. Fig. 1f, Kianfar et al. 2020). The right half of the CHROMIS FoV is quiet and therefore devoid of bright fibrils as shown in the Ca II K line-core image in Fig. 1a. We used this part of the FoV for the absolute intensity calibration of our observations (see Sect. 2.1).

3. Analysis methods

3.1. Measuring POS oscillations

In order to analyse transverse oscillations of bright fibrils visible in Ca II K we selected a region in our data that was observed by both CRISP and CHROMIS and contained fibrils (indicated by the white-dashed box in Fig. 1b). Then we defined 12 cuts of $3'' - 12''$ length perpendicular to the local orientation of the fibrils in this region. In space-time plots of the Ca II K line core intensity along these cuts, the fibrils appear as sinusoidal curves with a higher brightness than their surroundings (the top panel of Fig. 2 shows the space-time plot along the white dashed cut in Fig. 1f). We used the CRisp SPectral EXplorer computer program (CRISPEX; Vissers & Rouppe van der Voort 2012; Löfdahl et al. 2021) software to define and extract the cuts.

We defined the trajectory of the POS oscillations in the space-time plots using a combination of manual and automatic approaches: First, we visually defined a preliminary trail of an oscillation by choosing a sparse set of (x, t) points along a sinusoidal curve. Second, we interpolated in time between these points to get a continuous curve. Third, for each time step, we defined the location of the fibril as the point with the highest intensity within $\pm 0\farcs15$ around the interpolated trajectory. Finally, we smoothed the oscillation trajectories by applying a 1D boxcar average in time with a width of 64 seconds, to bring out the wave patterns and cancel out the small-scale fluctuations.

Using the above procedure enabled us to create a sample of 120 POS oscillations of Ca II K bright fibrils. The bottom panel of Fig. 2 shows the interpolated and smoothed trajectories of POS oscillations in the example cut marked in Fig. 1f. We calibrated the overall axis of the oscillations by subtracting a linear trend from the trajectories so that the oscillation axis becomes parallel to the time axis (Leenaarts et al. 2015). Then we computed the velocity of the POS oscillations by calculating the time-derivative of the amplitudes.

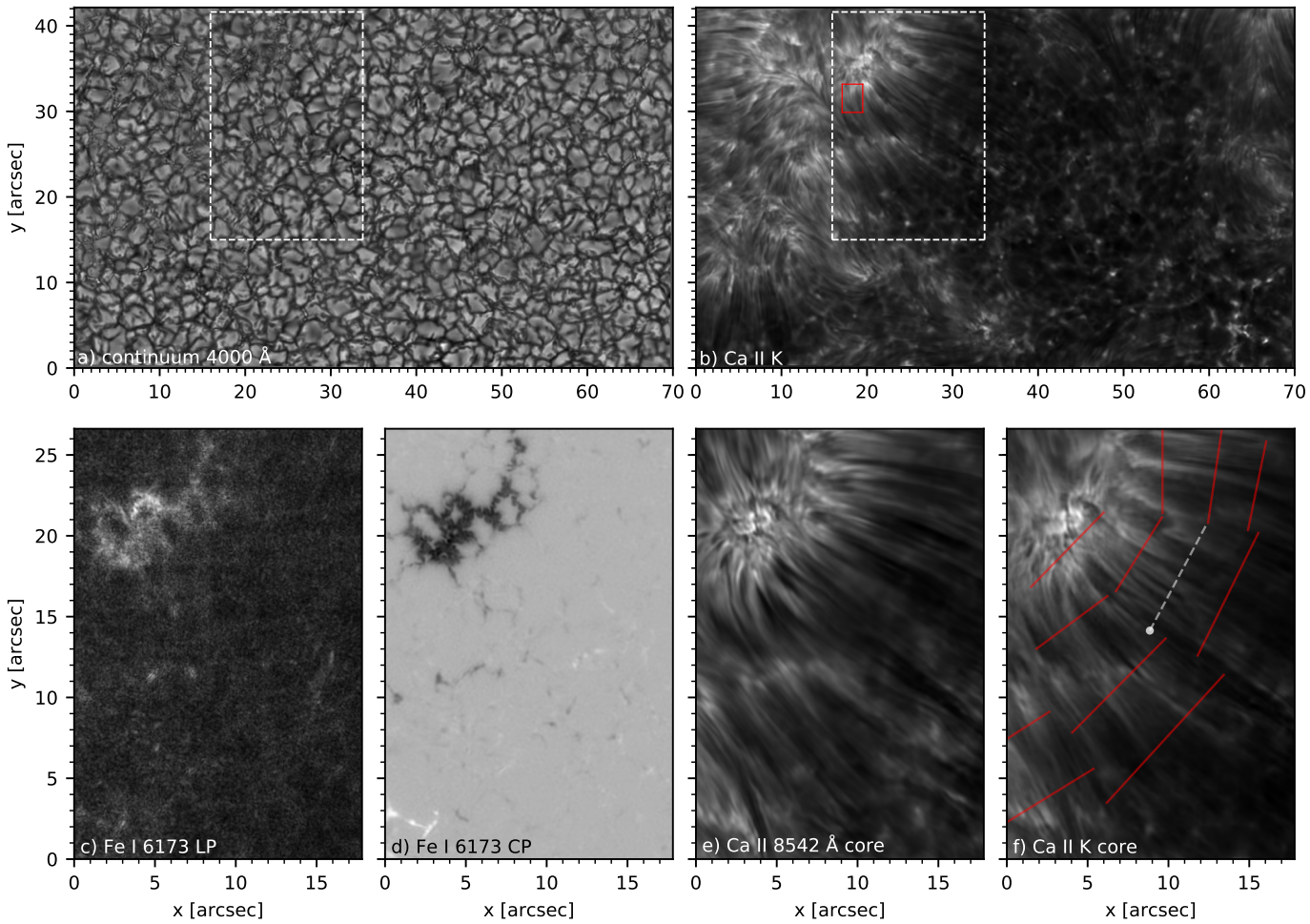

Fig. 1. Overview of the observations taken on 2018-07-22 at 08:31:49 UT. *Top panels* show intensity images of the continuum at 4000 Å (*a*) and the wavelength-integrated Ca II K line intensity (*b*). The white dashed box marks the region that we analyse in detail. The red box marks the RoI analysed in Fig 3. An zoom in of the area enclosed by the white dashed box is shown in the *bottom panels*. *c*: Fe I 6173 Å wavelength-averaged linear polarisation; *d*: Fe I 6173 Å wavelength-averaged circular polarisation; *e*: Ca II 8542 Å line core intensity; *f*: Ca II K line core intensity. The red solid and white dashed lines in panel *f* show the cuts across the Ca II K bright fibrils that we used (see Sec. 3.1). An analysis of the cut along the white dashed line is presented in Figs 7 and 8. The white dot marks the zero point on the *y*-axis in Fig. 7. An animated version of this figure showing the entire time sequence is available online.

3.2. Inversion and measurement of LOS oscillations

We used the MPI-parallel STockholm inversion Code (STiC; de la Cruz Rodríguez et al. 2019) to derive the physical properties of the atmosphere from our observations. We used the inferred atmospheric velocity to estimate the LOS velocity in our fibril sample.

To solve the polarised radiative transfer equation, STiC uses the radiative transfer code RH (Uitenbroek 2001) with Bezier solvers (de la Cruz Rodríguez & Piskunov 2013). STiC uses the equation-of-state that is acquired from the SME package functions (Piskunov & Valenti 2017), and includes partial redistribution (PRD) effects in the radiative transfer using the fast approximation method introduced in Leenaarts et al. (2012b). STiC fits multiple spectral lines simultaneously for each individual pixel by assuming the 1.5D approximation (i.e. plane-parallel atmosphere). We ran STiC on the observations of the three Fe I 6173 Å, Ca II 8542 Å, and Ca II K lines to retrieve the physical properties in both photosphere and chromosphere. In our inversion runs, we assumed the statistical equilibrium and non-LTE condition for Ca II, including partial redistribution for the Ca II H&K lines. For the Fe I 6173 Å line we assumed LTE.

We did not aim to determine the magnetic field, and therefore only fitted Stokes I, even though our observations included all four Stokes parameters for Fe I 6173 Å and Ca II 8542 Å. Because Zeeman broadening affects the width and shape of the line profiles, in particular for Fe I 6173 Å, we included the longitudinal magnetic field as a quantity in our atmospheric model with two nodes, and the transverse field with one node. Otherwise we used the same set-up and nodes to run the inversions as used in Kianfar et al. (2020), i.e., nine nodes in temperature, and four nodes for both $v_{\rm LOS}$ and $v_{\rm turb}$, located non-equidistantly in the optical depth span of $\log(\tau_{500\,\rm nm}) = [-7, 1]$. The inversion results are presented in Section 4.1.

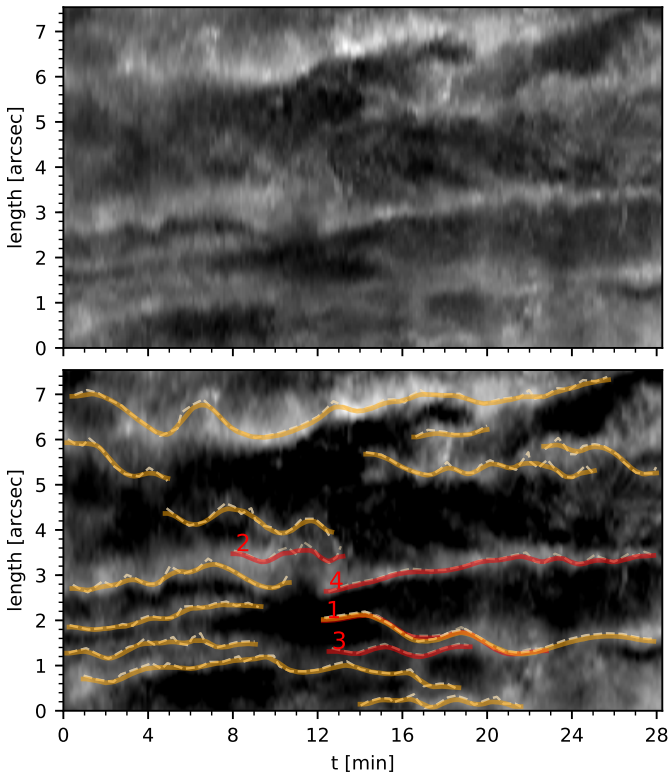

Fig. 2. Time evolution of the cut across the bright fibrils shown with white dashed line Fig. 1-f. *Top panel:* intensity at the nominal line centre of Ca II K. *Bottom panel:* contrast-enhanced space-time image of the intensity shown in the top panel. The oscillation trajectories of the bright fibrils in the POS are shown as dashed lines. The smoothed trajectories are plotted with solid curves. The oscillations properties of the curves marked with numbers are shown in Fig. 8. The zero point of the cut length (y-axis) is marked with a white dot in Fig. 1-f

.

4. Results

4.1. Inversion results

4.1.1. Region of interest

To study the time-evolution of the fibrils, we first ran inversions on the time-series of a 2D region of interest (RoI) marked by the red box in Fig. 1b. The results are shown in Fig. 3. The RoI covers an area of $3\farcs1 \times 2\farcs2$ centering on a long-lived fibril (Fig. 3, Ca II K image at 22 minutes) with a clear transverse oscillation. The temperature and $v_{\rm LOS}$ images in the photosphere (i.e. $\log(\tau_{500\,\rm nm}) = 0$) show a convection pattern consistent with the granulation pattern in the intensity images; there is higher temperature and upflows in the granules, and lower temperature and downflows in the intergranular lanes. The temperature in $\log(\tau_{500\,\rm nm}) = -3.9$ at $t = 10$ min and $t = 18$ min almost follows the fibrillar patterns of the intensity images at Ca II 8542 Å line-core. The fibrillar patterns in the temperature become more significant at $\log(\tau_{500\,\rm nm}) = -4.6$ in the chromosphere where the bright fibrils appear as temperature enhancements in agreement with the Ca II K intensity image (Kianfar et al. 2020). The upflow and downflow structures in the $v_{\rm LOS}$ images in the chromosphere do not particularly follow the fibrillar patterns, though they have the same average orientation as the fibrils (Kianfar et al. 2020).

We chose three perpendicular cuts (Fig. 3, $t = 22$ min) across the central fibril in the RoI. Figure 4 shows space-time plots of the intensity and inversion result along these cuts. The optical depth in which the inversion results are extracted is $\log(\tau_{500\,\rm nm}) = -4.3$ since the Ca II K line is most sensitive to the perturbations in the chromosphere at this optical depth (Kianfar et al. 2020). The smoothed interpolated trajectories of the fibrillar POS oscillations in the cross-cuts are defined by the method explained in Sect. 3.1 (overplotted curves in Fig. 4). They exhibit oscillations with a period P of about 8 minutes that last for two periods. The period stays constant along the fibril. We calculated the average phase speed for the oscillation along this fibril as

$$\bar{v}_\phi = \frac{\Delta r}{\Delta t_{\phi_c}}, \tag{1}$$

where Δr is the average distance between the cuts and Δt_{ϕ_c} is the average time difference between the two points with the same phase in the oscillations. Accordingly the wave along this fibril propagates with a speed of $\sim$13 km s^{-1} from cut(1) to cut(3). The amplitude of the oscillations is highest ($A_1 \approx 0\farcs5$) at the head of the fibril (i.e. close to the magnetic field concentration, top panels of Fig. 4) and it decreases to $A_3 \approx 0\farcs2$ in the tail.

The temperature (middle column of Fig. 4) almost follows the oscillatory patterns in intensity with enhancements of 40–60 K. There are no obvious wave patterns in $v_{\rm LOS}$.

We extracted the temperature and $v_{\rm LOS}$ along the POS oscillations in the cuts of Fig. 4 in the atmosphere between $\log(\tau_{500\,\rm nm}) = [-6, -2]$. This is roughly the height range where Ca II K line responds to perturbations of the physical properties in the atmosphere (Kianfar et al. 2020). The results are shown in Fig. 5. The oscillatory pattern in $v_{\rm LOS}$ (right panel) starts around $\log(\tau_{500\,\rm nm}) \sim -3$ and gets larger at larger heights and peaks between $\log(\tau_{500\,\rm nm}) = [-3, -6]$. The temperature profiles (left panel) do not show any particular wave patterns.

However, there are peaks forming at $t = 11$ and 19 minutes, i.e, where the POS amplitude has extrema (see Fig. 4). These temperature peaks start appearing around $\log(\tau_{500\,\rm nm}) = -3.5$ and get stronger up to $\log(\tau_{500\,\rm nm}) = -5$. Higher up they get damped. This height range is where bright Ca II K fibrils show temperature enhancements compared to their surroundings (Kianfar et al. 2020).

While the peaks in the temperature profiles get smaller as we move towards the tail of the fibril (i.e., from cut 1 to cut 3), the amplitude of $v_{\rm LOS}$ oscillations increases. Figure 6 shows a comparison of the time evolution of T and $v_{\rm LOS}$ at $\log(\tau_{500\,\rm nm}) = -4.31$ to $v_{\rm POS}$. It shows that both the temperature variation and its average decrease as we move from the head to the tail of the fibril. The amplitude of $v_{\rm POS}$ behaves the same. The $v_{\rm LOS}$ curves show different behaviour, with the highest amplitude peak at about $t = 17$ min in cut (3), i.e., close to the tail of the fibril. We further discuss the $v_{\rm POS}$ and $v_{\rm LOS}$ oscillations of our sample and their wave properties in Sect. 4.2.

4.1.2. Cross-cuts

Figure 7 shows the temperature and $v_{\rm LOS}$ of the example cut shown Fig. 2 at two chromospheric heights. The temperature in the lower chromosphere ($\log \tau_{500} = -3.5$) barely shows fibrillar structures. Higher up, at $\log \tau_{500} = -4.31$, the temperature image shows a similar pattern to the intensity space-time image (Fig. 2) with enhanced temperature at the location of the bright fibrils (Kianfar et al. 2020). The $v_{\rm LOS}$ space-time images do not demonstrate a clear correlation to the fibrillar oscillation trajectories in the POS and appears similar at both heights, with only a slight difference in the range of the velocity values.

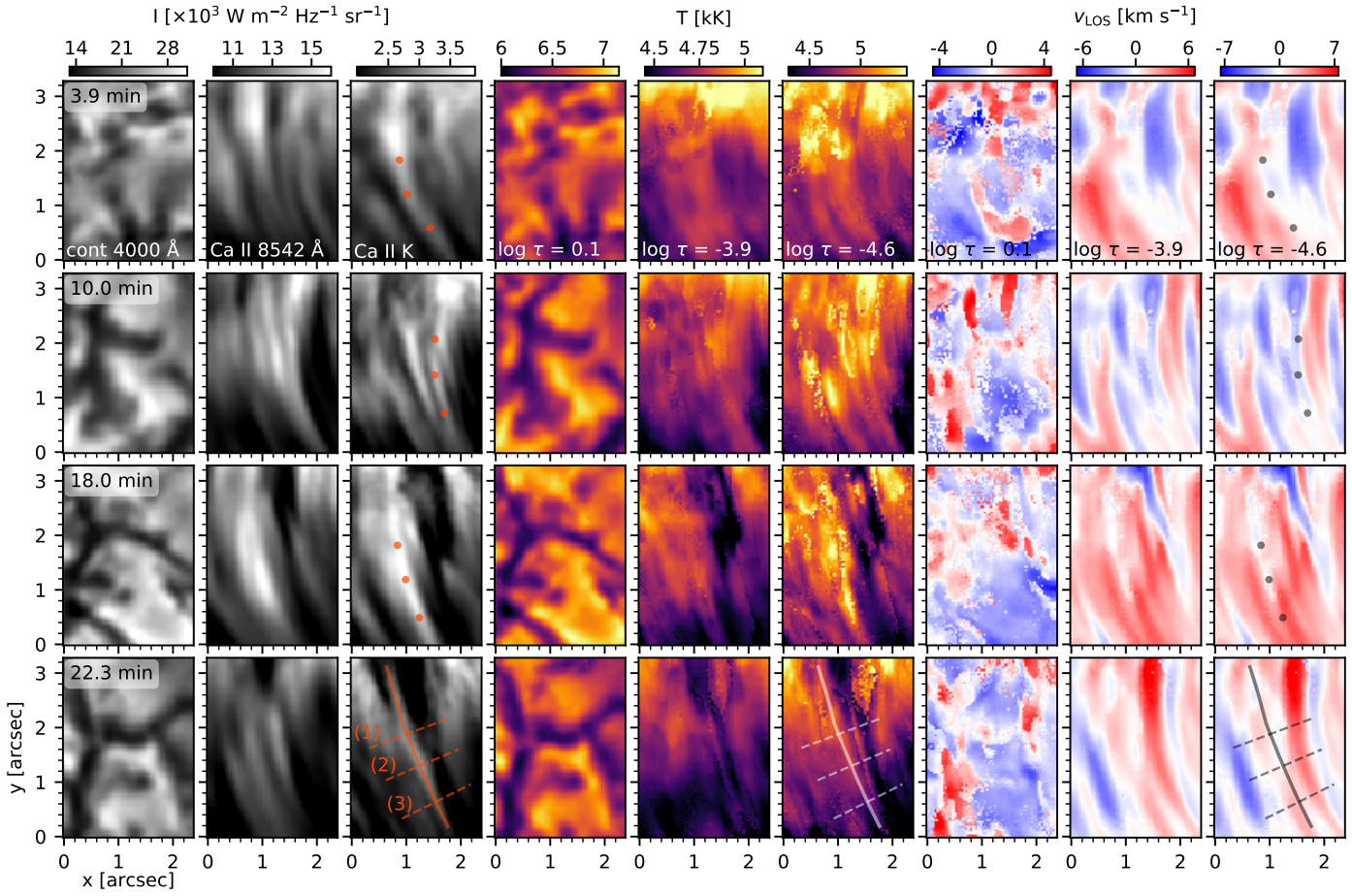

Fig. 3. Time evolution of the physical properties of the RoI marked with a red box in Fig. 1. *Left panels:* intensity variation over time (from top to bottom) at the 4000 Å continuum, and in the line cores of Ca II 8542 Å and Ca II K. *Middle* and *right panels:* time evolution of the temperature and v_{LOS} at a photospheric depth ($\log(\tau_{500\,nm}) = 0.1$) and two different chromospheric depths, $\log(\tau_{500\,nm}) = -3.9$ and -4.6. One specific fibril in the RoI is marked in the 22 minute panel of the Ca II K intensity. Three cuts across the head, middle and the tail of this fibril are marked and numbered and their properties as function of time are displayed in Fig. 4. The red and grey dots indicate where the three cuts cross this specific fibril at different times of its evolution.

4.2. 3D oscillations

From the POS oscillation trajectories (Sect. 3.1) and space-time inversion results of the cuts across the fibrils (Sect. 4.1.2), we determined the LOS velocity along the fibrils; we extracted the v_{LOS} values along the smoothed trajectory of the POS oscillations (Sect. 3.1) at $\log(\tau_{500\,nm}) = -4.31$, i.e. the height where temperature and velocity at fibrillar locations are most sensitive to the perturbations in the chromosphere (Kianfar et al. 2020). We compute the velocity in the POS by taking the time derivative of the POS displacement. The top panels of Fig. 8 show v_{LOS} an v_{POS} along the four example fibrils marked with numbers in Fig. 2.

4.2.1. Determination of the oscillation properties

We derived the wave properties in our oscillation sample through a combination of automatic and manual approaches. First, we computed the autocorrelation of each v_{LOS} and v_{POS} curve. Besides the peak at a time lag $\Delta t = 0$ s, a curve with an oscillation shows a secondary peak at a time lag roughly equal to the dominant period of the oscillation. Because the velocity curves contain noise, and might contain partial oscillations, interference patterns or oscillation with changing period, the secondary peak can have a much lower amplitude. Combined with visual inspection, we selected 118 fibrils that have a clear oscillation in both v_{LOS} and v_{POS}. The middle panels of Fig. 8 show the autocorrelations for the four example fibrils marked with numbers in Fig. 2.

We then derived periods for this subsample by measuring the time of each extremum, and compute "partial periods" as the time difference between two consecutive minima or maxima. As the periods are not constant throughout one oscillation, we assigned an average and a dominant period ($\bar{P}$, P_{dom}) as the mean and maximum of the partial periods for v_{LOS} and v_{POS} in each fibril. We also measured the amplitude of each extremum, and used that to assign an average amplitude $\bar{A}$ for v_{LOS} and v_{POS} in each fibril.

To quantify the correlation between v_{LOS} and v_{POS}, we calculated the normalised cross-correlation function, $\hat{C}(t)$, for each fibril. Example cross-correlation curves are shown in the bottom panels of Fig. 8. We considered fibrils with $max\{|\hat{C}(t)|\} > 0.5$ as potentially exhibiting correlation motion. Then we visually inspected those fibrils to confirm that v_{LOS} and v_{POS} indeed had similar periods and oscillation patterns. The differences in period between the two velocity components is smaller than 22%. We found that 55 fibrils out of the 118 showed correlated oscillations. For this subset we computed the phase difference between

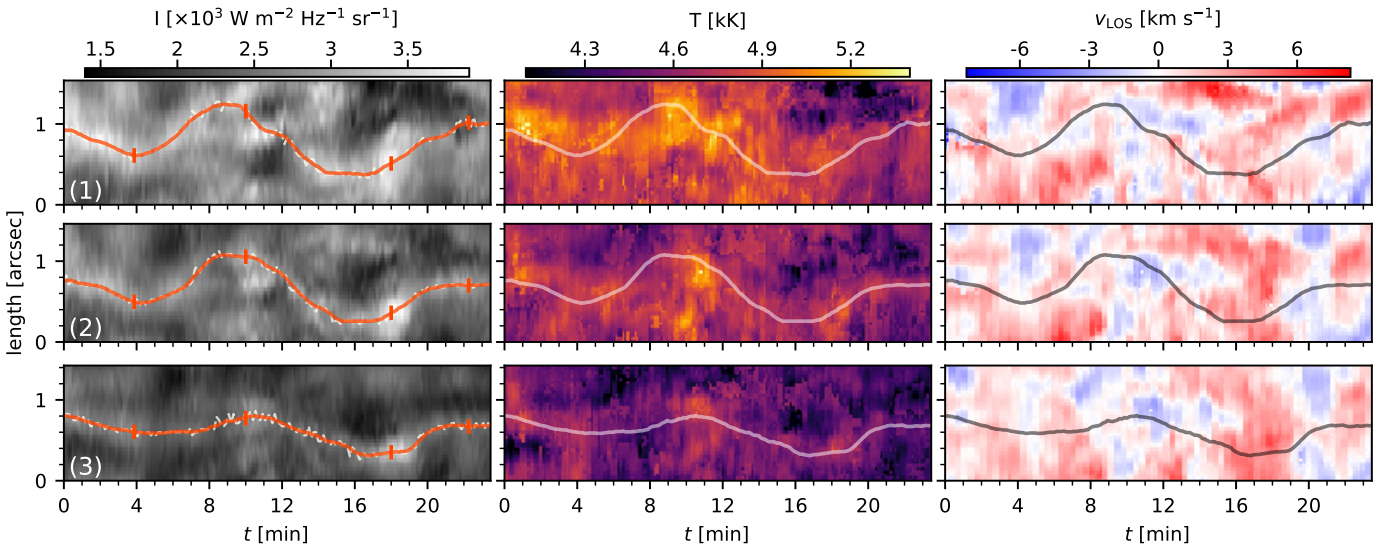

Fig. 4. Physical properties of the cuts perpendicular to the bright Ca II K fibril marked in Fig. 3. *Left column* shows the intensity-over-time variations of the cuts at Ca II K nominal line centre. The oscillation in the POS is visually tracked and marked by red curves. *Middle* and *right columns* demonstrate the temperature and $v_{\rm LOS}$ variations of the cuts as function of time in the chromosphere ($\log(\tau_{500\,\rm nm}) = -4.31$). The POS oscillation is overplotted on these images as well. Length zero on the y-axis is where the cuts are marked by numbers in Fig. 3.The | symbols, marked on the curves in the left column, show the times of the fibril's evolution that are displayed in Fig. 3.

Table 1. LOS and POS fibril oscillation properties

	min	max	mean	std. dev.
$\overline{P}_{\rm POS}$ (s)	118	607	218	87
$\overline{P}_{\rm LOS}$ (s)	91	635	195	78
$\overline{A}_{\rm POS}$ (km s^{-1})	0.25	7.9	1.9	1.0
$\overline{A}_{\rm LOS}$ (km s^{-1})	0.17	2.7	1.1	0.45

the oscillations as

$$\Delta\phi = \pi\frac{\Delta t}{P_M}, \quad -\pi \le \Delta\phi \le \pi, \tag{2}$$

where $P_M = (\bar{P}_{\rm LOS} + \bar{P}_{\rm POS})/2$. The online animation accompanying Fig. 8 shows all fibrils in our sample.

4.2.2. Statistical analysis

Figure 9 shows the distribution of and correlations between the measured periods and amplitudes. Table 1 shows their minimum maximum, average, and standard deviation.

The top-left panel of Fig. 9 shows a weak but positive correlation between the $\overline{P}_{\rm POS}$ and $\overline{P}_{\rm LOS}$ especially between periods of 150 to 250 s. In contrast, the amplitudes (lower-left panel) do not appear to have a correlation between the two POS and LOS directions. In general the $v_{\rm LOS}$ oscillations tend to have smaller amplitudes compared to $v_{\rm POS}$, instead. This is also confirmed by the mean values in Table. 1. There appears to be no correlation between the amplitude and period in the POS direction (upper right), and likewise for the LOS direction (lower right).

We show the distribution of the phase difference between the $v_{\rm POS}$ and $v_{\rm LOS}$ oscillations for the 55 fibrils in our sample that show correlated velocity oscillations in the POS and LOS directions in Figure 10. The observed phase difference span the whole range of $[-\pi, \pi]$. This implies that the total velocity vectors $\mathbf{v}_{tot} = (v_{\rm POS}, v_{\rm LOS})$ can range from fully linearly polarized ($\Delta\phi = 0$, $-\pi$, or π) to fully circularly polarized ($\Delta\phi = \pm\pi/2$).

We also show the distribution of $|\Delta\phi|$ in Fig. 10. Because our sample size is limited and we are only interested in absolute phase differences, this lowers the statistical noise in our sample. There is a clear peak in the distribution for linearly polarized waves, and there is a hint of a secondary peak for fully circularly polarized waves in the $|\Delta\phi|$ distribution.

In order to visualize the motion of the spicule axes we integrated the LOS velocity to obtain the LOS displacement as a function of time. Together with the measured POS amplitude we can then trace the motion of a particular point along a fibril as a function of time. We display these curves for the four example fibrils shown in Figs. 2 and 8 in Fig. 11.

The phase differences between the velocity oscillations of the examples (1) and (2) are 0 and π as shown in Fig. 8, suggesting a linear polarized wave. This linear behaviour is seen roughly in the total motion of the example (2) in Fig. 11 but not so clearly in example (1). Example (3) has a $\Delta\phi \approx \pi/2$, and the projection of the amplitude vector traces out an elliptical path. Example (4) has velocities that appeared to have low-ampitude short-period velocities with different periods in the LOS and POS directions. However, the projection of the amplitude vector reveals it carried a long-period linear oscillation as well as the short period oscillations.

Finally, we investigated the spatial distribution of the periods and phase differences. Our results are shown in Fig. 12. Longer period oscillations (> 200 s) tend to occur preferentially closer to the fibril footpoints in the network patch. Further away from the network we detect mainly short-period oscillations (< 200 s). The phase differences do not show an obvious trend. The cases where there are no oscillations in the LOS direction (shown by × symbols) are very few and all far from the magnetic concentrations.

Summary of results We summarise our main findings: we selected a number of cross cuts through Ca II K bright fibrils, and identified a sample of 120 fibrils along these cross-cuts. We determined the velocity amplitudes and periods of the fibril oscil-

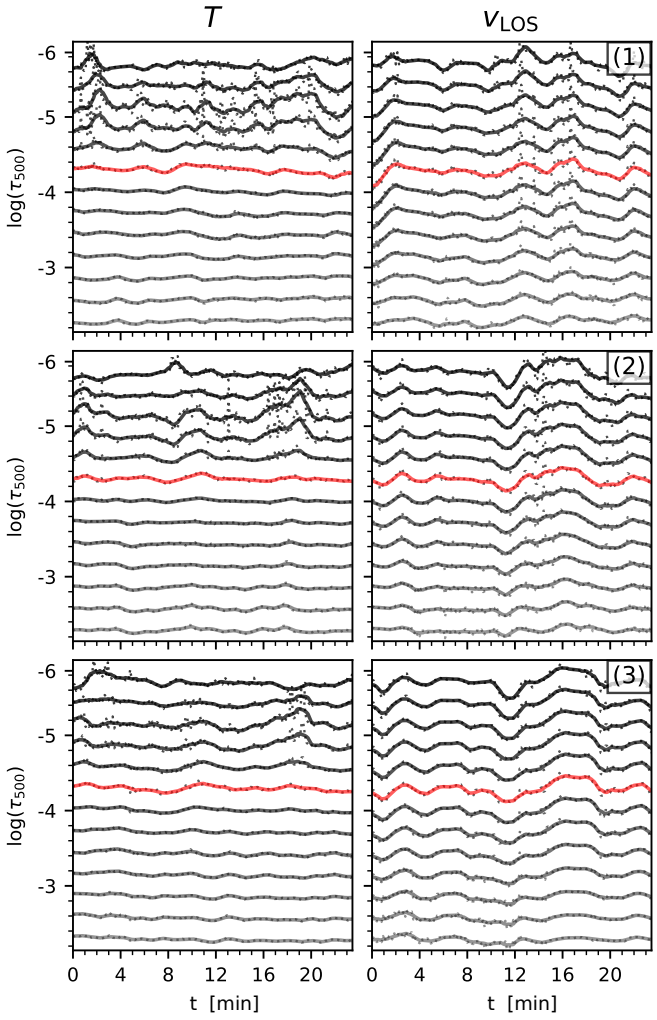

Fig. 5. Temperature and v_{LOS} variations of the three cuts marked in Fig. 3 over time. *Left* and *right column* show the temperature and v_{LOS} variations along the POS oscillation trajectory (marked in Fig. 4) for a depth range where Ca II K is sensitive to the perturbations in the atmosphere. Solid curves are the smoothed plots of the actual values that are shown with dots. Red-colored plots mark the depth where Ca II K has the highest sensitivity to atmospheric perturbations. These curves are plotted individually in Fig. 6.

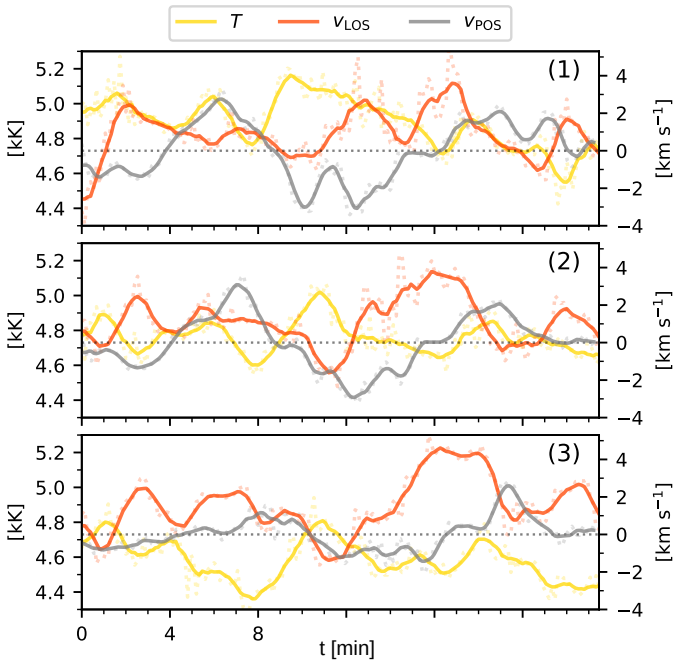

Fig. 6. Variations of the temperature (*left column*) and v_{LOS} (*right column*) of the perpendicular cuts across the fibril shown in Fig. 3. They are plotted based on their values extracted along the oscillation trajectory in POS marked in Fig. 4 at the depth $\log(\tau_{500\,nm}) = -4.31$ (i.e. where the Ca II K line is most sensitive to atmospheric perturbations). Oscillation of the v_{POS} is plotted in gray for comparison on the panels in the *right column*.

lations for both the LOS and POS directions. The distribution of periods in both directions is very similar, with a mean period of around 2.2×10^2 s. The mean velocity amplitude in the POS direction is however almost twice as large (1.9 km s^{-1}) as in the LOS direction (1.1 km s^{-1}).

Because the sample was selected based on POS oscillations, all of them exhibit a POS oscillation. Almost all of them (118) also show a clear LOS oscillation pattern. Of those, 55 fibrils showed oscillations with similar periods in both the LOS and POS directions. For these, we measured the phase difference between the two oscillation directions. All phase differences occur, but there is a preference for zero phase difference, and possibly a slight preference for a 90-degree phase difference.

5. Discussion

The periods and POS velocity amplitudes that we measure here fall in the range of transverse oscillations observed in Hα fibrils as reported by Morton et al. (2013). The oscillations in Hα spicule-like events reported by Shetye et al. (2021) have smaller periods and larger amplitudes.

The mean period that we observe is more than twice as large as the values reported in Jafarzadeh et al. (2017b) for Ca II H fibrils observed with a 0.11 nm filter. Table 2 of Jafarzadeh et al. (2017b) list observed periods and amplitudes of transverse oscillations in fibrils, mottles, and spicules observed in Hα and Ca II H in different studies using a variety of instruments. The observed periods range between 16 s and 600 s, roughly consistent for all studies. However, the differences in periods and amplitudes might be caused by differences in observed target, observing cadence, different methods to define and detect spicules, and different data processing. A limit of our study is that we smooth oscillations in time with a 64 s boxcar average, with effectively blocks us from detecting periods smaller than $\sim$ 120 s, which might explain the larger value for the mean period that we found compared to those in Jafarzadeh et al. (2017b) and Shetye et al. (2021).

The range of velocity amplitudes varies, with observations of fibrils in Hα and Type II spicules having median values of 5 km s^{-1} to 10 km s^{-1}. The Ca II K fibrils in this study, as well as those observed by Jafarzadeh et al. (2017b) have a POS velocity amplitude of roughly 2 km s^{-1}. This difference could be explained by the differences in formation height together with decreasing mass density with height: for constant wave flux (and phase speed), lower density gas implies larger velocity amplitude.

For fibrils that appear both in Ca II K and Hα, the segment of the fibril that appears bright in Ca II K is likely located lower in the atmosphere than the segment visible in Hα. Kian-

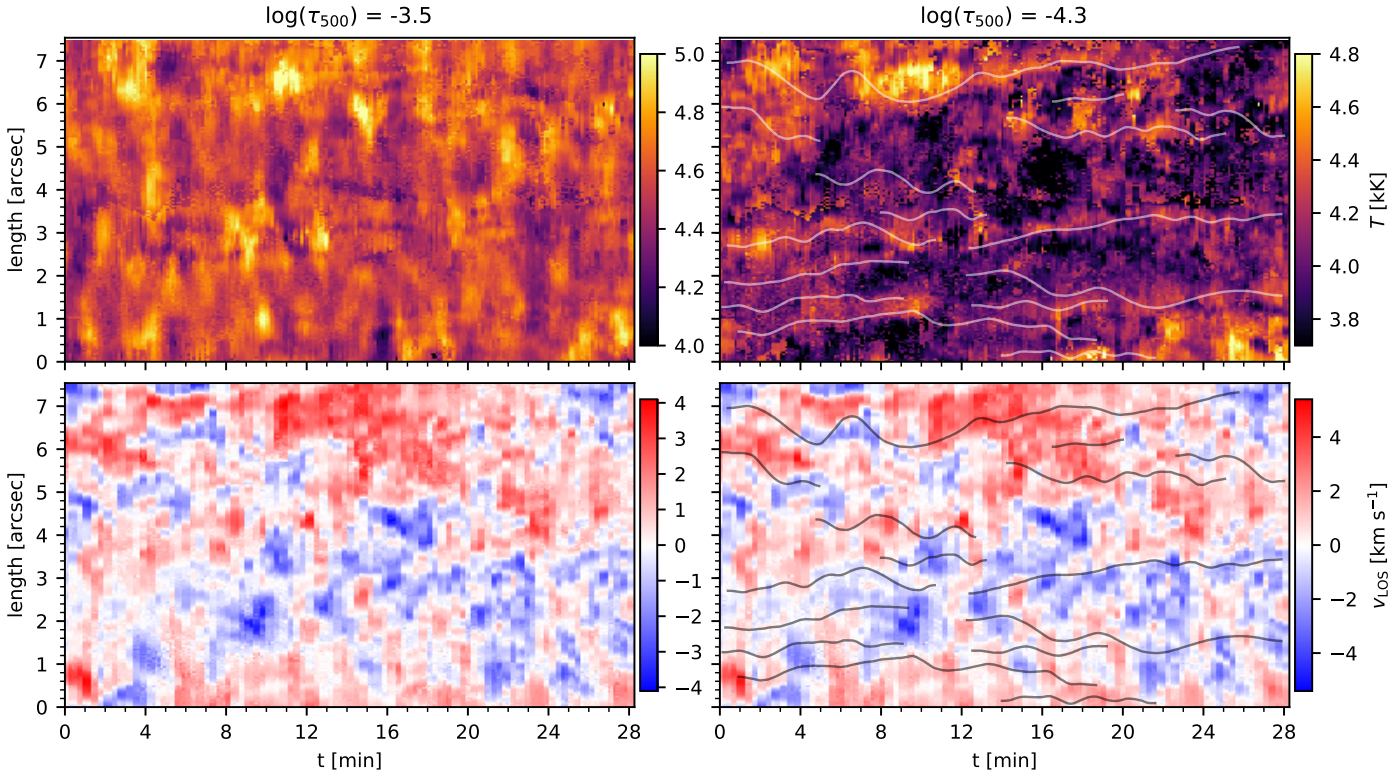

Fig. 7. Time evolution of the physical properties of the example cross-cut shown in Fig. 2. *Left column* shows the inversion results at lower chromosphere and the *right column* represents the results in higher chromosphere. *Top panels* show the temperature of the cut in the chromosphere. *Bottom panels* are space-time images of line-of-sight velocity. The POS oscillations are overplotted on the *right panels*. Zero point of the cut length is marked with a white dot in Fig. 1.

far et al. (2020) showed that Ca II K shows fibrils located around $\log \tau_{500} \approx -4.3$, while the H$\alpha$ line core forms at larger heights ($\log \tau_{500} \approx -5.7$ in the FALC model atmosphere). Type II spicules can protrude far above the bulk chromosphere and are expected to form at even lower densities.

The presence of oscillation with comparable periods in the LOS and POS direction for 55 out of 118 fibrils in our sample strongly indicates that both oscillation directions are excited by the same process. Theoretical calculations show that curved flux tubes have nearly the same wave speeds in the vertical and horizontal directions (van Doorsselaere et al. 2009).

We interpret the presence of fibrils with identical periods and zero phase difference in our sample as evidence of convective buffeting (Spruit 1981) with randomly oriented kicks as a driver because there is no obvious correlation between the LOS and POS velocity amplitudes (Fig. 9). Simulations of photospheric magnetoconvection at high resolution (e.g. Rempel 2014) show however substantially more complex motions of photospheric magnetic elements, which could explain the whole range of phase differences that we observe.

We note that we detect oscillations with periods longer than 200 s preferentially close to the network patch that makes up the footpoint region of our fibril sample (Fig. 12). Further away we find mainly shorter periods. This hints at an alternative driving mechanism: buffeting of the fibrils from below by quiet-Sun 3-min slow-mode oscillations. Idealized simulations by Rosenthal et al. (2002), as well as more complex simulations by Nutto et al. (2012) indicate that such waves can convert into the fast mode with a component of its velocity amplitude transverse to the magnetic field. We might well detect such oscillations in our fibrils far from the network.

We measure an average velocity amplitude in the POS direction of 1.9 km s^{-1}, almost twice as large as the 1.1 km s^{-1} measured in the LOS direction. This difference could be due to the difference in measurement technique: we determine POS amplitudes from measuring fibril tracks in images, while we infer the LOS amplitude through non-LTE inversions. The inversions assume a smooth velocity profile as a function of height, with only four nodes. In addition, the inversion includes microturbulence, which is of the order of 2.5 km s^{-1} in fibrils (Kianfar et al. 2020). There is some degeneracy between the velocity and the microturbulence, which might lower the inferred velocities, especially given our relatively coarse velocity resolution.

Similarly, Shetye et al. (2021) find smaller LOS amplitudes than POS amplitudes in Hα spicules. They define the LOS velocity as the first moment of the line profile, which can yield different values than the actual LOS gas velocity (see Figs. 5 and 6 in Danilovic et al. 2022). Measurement of fibril oscillations in Hα using the Doppler shift of the line profile minimum as a LOS velocity measurement (Leenaarts et al. 2012a) could provide a more reliable measurement of the relative sizes of the LOS and POS velocity amplitudes.

We find a hint of a preference for phase differences of $\pi/2$, indicative of fully circularly polarized waves, in the context of flux tubes known as helical kink waves (Zaqarashvili & Skhirtladze 2008). This leads to circular motion of the tube axis in the plane perpendicular to the tube. Such motions have been detected before in both off-limb spicules (e.g., Gadzhiev & Nikolskii 1982) and on-disk spicules (Shetye et al. 2021). Similar mo-

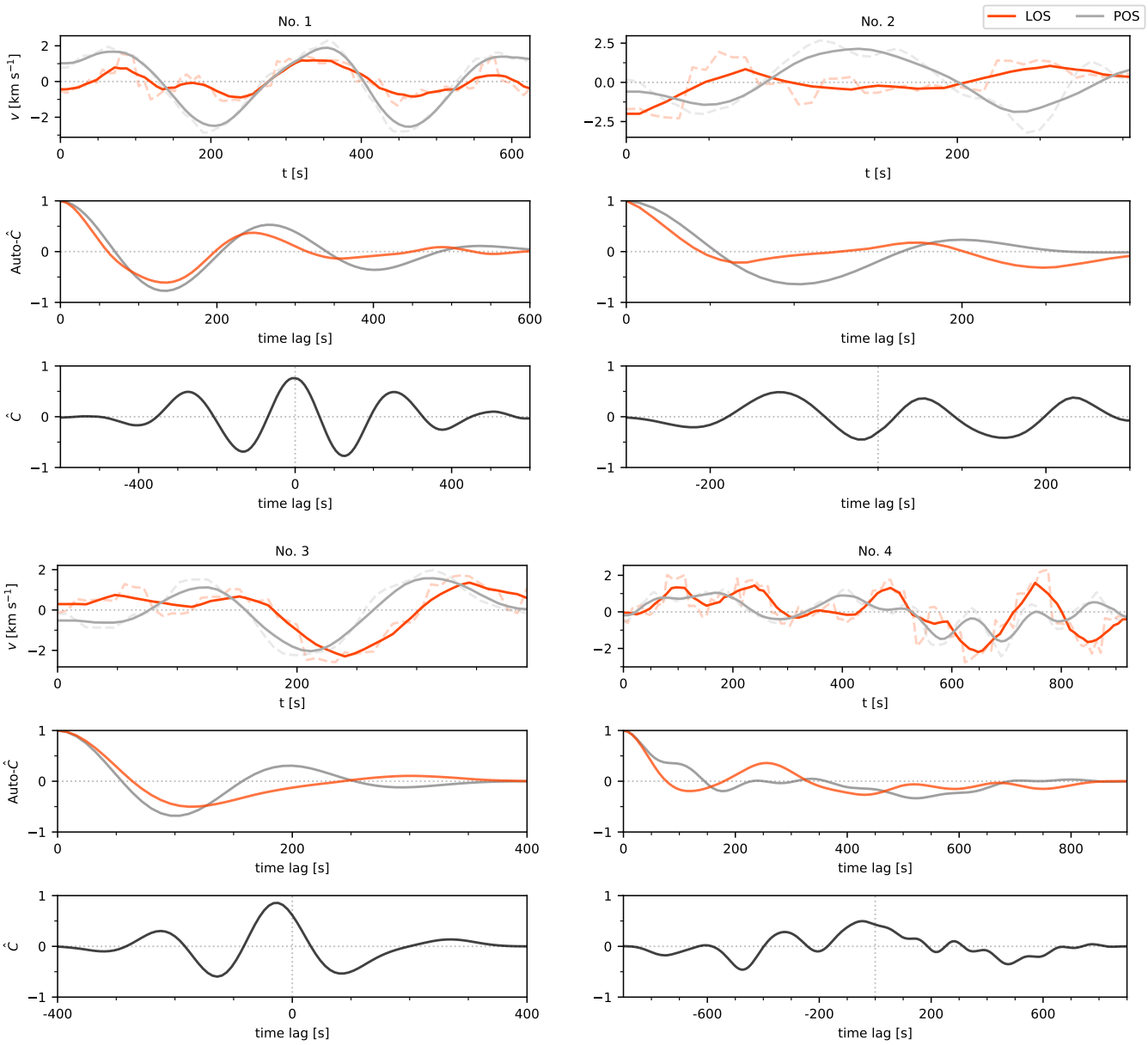

Fig. 8. Comparison of the velocity oscillations of the examples marked with numbers in Fig. 2. These examples represents four different groups of oscillations in our sample of Ca II K fibrillar oscillations. *Top plot* of each panel, shows the oscillation of velocity in the plane-of-sky (red curve), compared to the velocity oscillation along the line-of-sight direction (grey curve). *Middle plots* of the panels show the results of the auto-correlation calculation on both POS and LOS velocity oscillations. Normalised products of auto-correlations, i.e. normalised cross-correlation ($\hat{C}$ function) of the POS and LOS velocity oscillations are shown in the *bottom plots* of the panels. For the interpretation of the above plots and more details on the different fibrillar groups see Sect. 4.2.1 and 4.2.2. An animation of this figure is available online that shows all 118 fibrils in the sample.

tions have also been detected in the chromosphere above photospheric magnetic elements using feature tracking (Stangalini et al. 2017).

Finally, we note that estimates of the wave flux carried by transverse waves in chromospheric fibrils based on POS motions only are an underestimate because they do not include the significant LOS motions. As we show here, imaging spectroscopy together with non-LTE inversions is a powerful tool to study chromospheric oscillations in all three dimensions.

Acknowledgements. SK and JL were supported through the CHROMATIC project (2016.0019) funded by the Knut and Alice Wallenberg foundation. SEP was supported by the Knut and Alice Wallenberg Foundation and also acknowledges the funding received from the European Research Council (ERC) under the European Union's Horizon 2020 research and innovation program (ERC Advanced Grant agreement No.742265). SD has received funding from Swedish Research Council (2021-05613) and Swedish National Space Agency (2021-00116). The Swedish 1-m Solar Telescope is operated on the island of La Palma by the Institute for Solar Physics of Stockholm University in the Spanish Observatorio del Roque de los Muchachos of the Instituto de Astrofísica de Canarias. The Institute for Solar Physics is supported by a grant for research infrastructures of national importance from the Swedish Research Council (registration number 2021-00169). This project has received funding from the European Research Council (ERC) under the European Union's Horizon 2020 research and innovation program (SUNMAG, grant agreement 759548). The NSO is operated by the Association of Universities for Research in Astronomy, Inc., under cooperative agreement with the National Science Foundation.

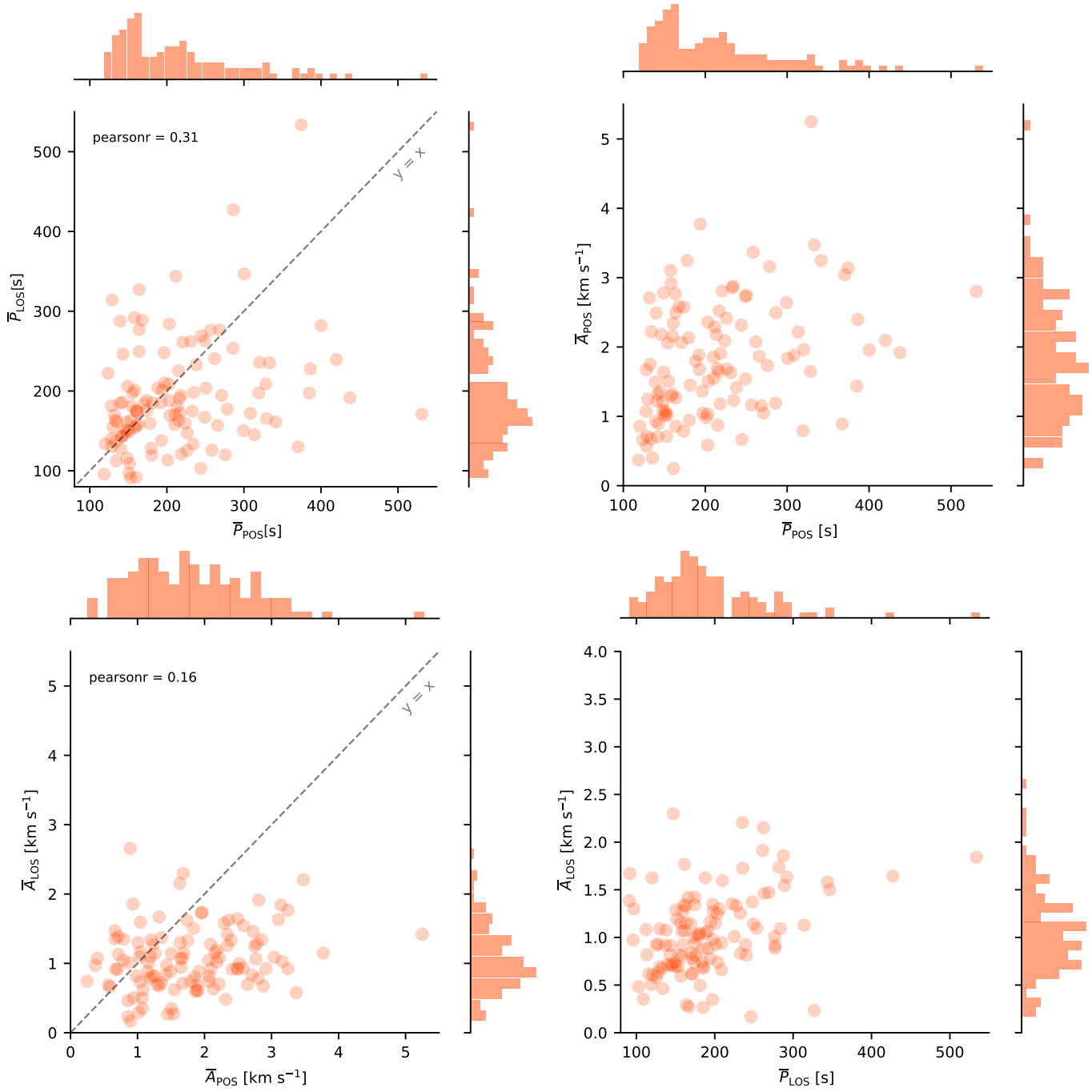

Fig. 9. Scatter plots and histograms of the average period $\bar{P}$ and average amplitude $\bar{A}$ of the 118 fibrils in our sample that show POS and LOS oscillations. The panels show scatter plots of the quantities indicated in the axis labels. The histogram distribution for each quantity is shown in the side-plots corresponding to their axis. The Pearson correlation coefficient r is annotated in the corner of the left-hand panels.

References

Antolin, P., Schmit, D., Pereira, T. M. D., De Pontieu, B., & De Moortel, I. 2018, ApJ, 856, 44
Bjørgen, J. P., Leenaarts, J., Rempel, M., et al. 2019, A&A, 631, A33
Carlsson, M., De Pontieu, B., & Hansteen, V. H. 2019, ARA&A, 57, 189
Carlsson, M. & Stein, R. F. 1997, ApJ, 481, 500
Danilovic, S. 2022, arXiv e-prints, arXiv:2208.03744
Danilovic, S., Bjørgen, J. P., Leenaarts, J., & Rempel, M. 2022, arXiv e-prints, arXiv:2208.13749
de la Cruz Rodríguez, J., Leenaarts, J., Danilovic, S., & Uitenbroek, H. 2019, A&A, 623, A74
de la Cruz Rodríguez, J., Löfdahl, M. G., Sütterlin, P., Hillberg, T., & Rouppe van der Voort, L. 2015, A&A, 573, A40
de la Cruz Rodríguez, J. & Piskunov, N. 2013, ApJ, 764, 33
De Pontieu, B., Carlsson, M., Rouppe van der Voort, L. H. M., et al. 2012, ApJ, 752, L12
De Pontieu, B., McIntosh, S. W., Carlsson, M., et al. 2007, Science, 318, 1574
Edwin, P. M. & Roberts, B. 1983, Sol. Phys., 88, 179
Gadzhiev, T. G. & Nikolskii, G. M. 1982, Soviet Astronomy Letters, 8, 341
Goossens, M., Terradas, J., Andries, J., Arregui, I., & Ballester, J. L. 2009, A&A, 503, 213
Jafarzadeh, S., Solanki, S. K., Gafeira, R., et al. 2017a, ApJS, 229, 9
Jafarzadeh, S., Solanki, S. K., Gafeira, R., et al. 2017b, ApJS, 229, 9
Jess, D. B., Morton, R. J., Verth, G., et al. 2015, Space Sci. Rev., 190, 103
Kianfar, S., Leenaarts, J., Danilovic, S., de la Cruz Rodríguez, J., & José Díaz Baso, C. 2020, A&A, 637, A1
Kuridze, D., Morton, R. J., Erdélyi, R., et al. 2012, ApJ, 750, 51
Leenaarts, J., Carlsson, M., & Rouppe van der Voort, L. 2012a, ApJ, 749, 136
Leenaarts, J., Carlsson, M., & Rouppe van der Voort, L. 2015, ApJ, 802, 136

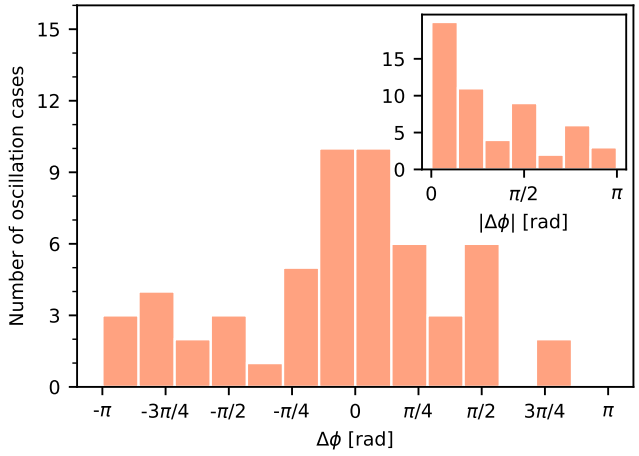

Fig. 10. Distribution of the phase difference $\Delta\phi$ and $|\Delta\phi|$ for the 55 fibrils in our sample that show velocity oscillations in the POS and LOS direction with similar periods.

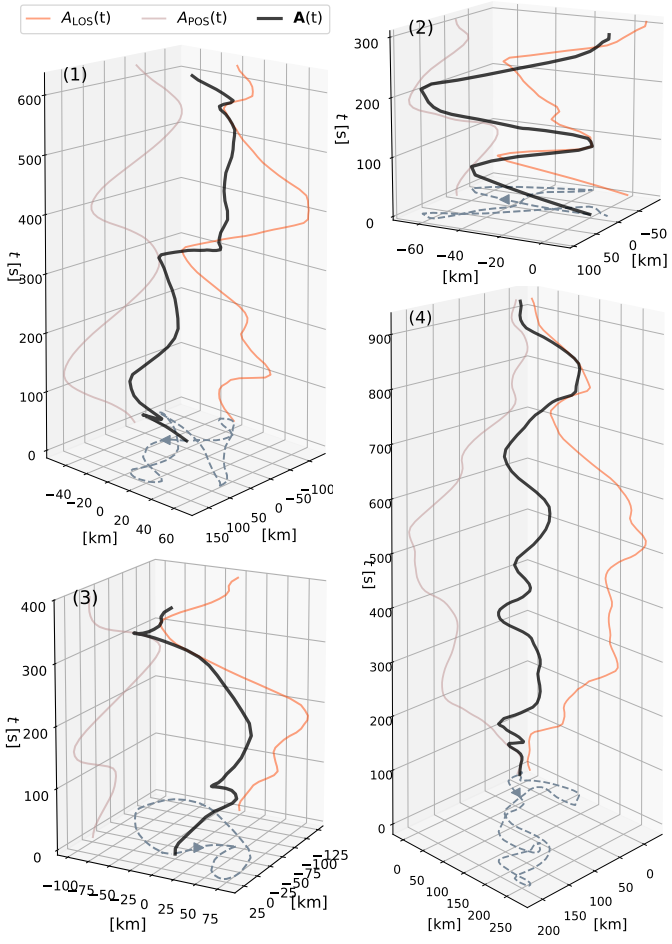

Fig. 11. Time evolution of the motion of a point along the spicule axis $\mathbf{A}(t)$ of the four example oscillations shown in Figs. 2 and 8. The oscillations in POS and LOS are shown in the side planes and the projections of the total motions are plotted in the plane perpendicular to the POS and LOS. The small arrow shows the direction of the motion in the bottom plane. An animated version of this figure is available online.

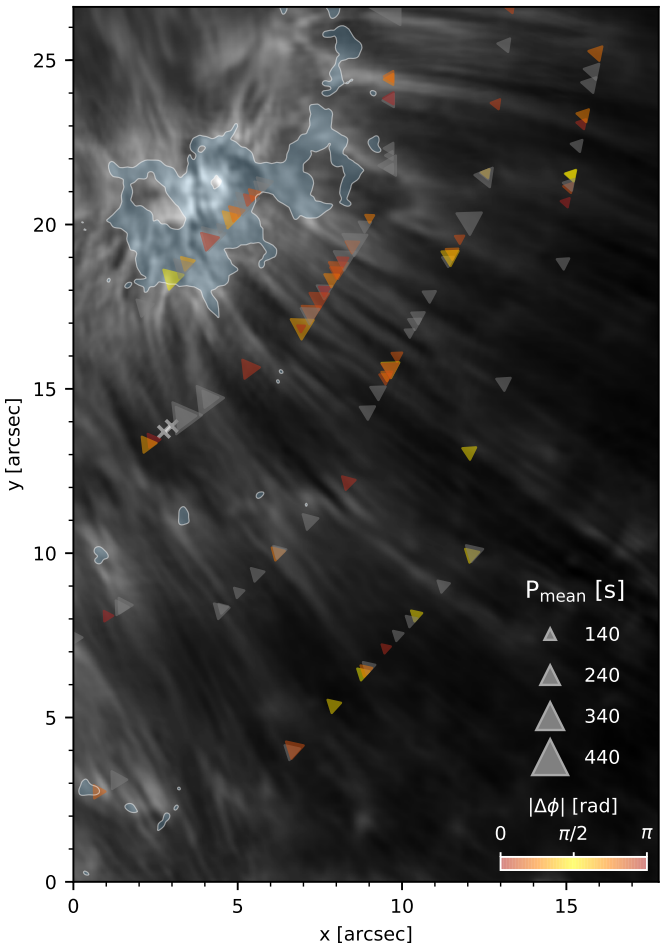

Fig. 12. Spatial distribution of measured fibril oscillation periods and LOS-POS phase differences. Each symbol marks the coordinates of the oscillation point. The ▲ symbols mark the points where an oscillation is detected in both v_{POS} and v_{LOS}. The size of the ▲ symbols is proportional to their average period. The color-coding of yellow, orange and red represents the absolute values of the phase difference between the v_{LOS} and v_{POS} oscillations where their period is correlated. The coordinates of the oscillations that do not have a clear correlation between their $\overline{P}_{POS}$ and $\overline{P}_{LOS}$ are shown with gray triangles. The orientation of the ▲ symbols show the perpendicular direction to the cuts (Fig. 1-f) across the bright fibrils. The cross symbols mark the points where an oscillation is detected in the POS direction but not in the LOS direction. The white filled contour lines indicate areas in the photosphere with magnetic concentrations, where the footpoints of the fibrils are located.

Leenaarts, J., Pereira, T., & Uitenbroek, H. 2012b, A&A, 543, A109
Löfdahl, M. G., Hillberg, T., de la Cruz Rodríguez, J., et al. 2021, A&A, 653, A68
Morton, R. J., Verth, G., Fedun, V., Shelyag, S., & Erdélyi, R. 2013, ApJ, 768, 17
Morton, R. J., Verth, G., Hillier, A., & Erdélyi, R. 2014, ApJ, 784, 29
Neckel, H. & Labs, D. 1984, Sol. Phys., 90, 205
Nutto, C., Steiner, O., Schaffenberger, W., & Roth, M. 2012, A&A, 538, A79
Pietarila, A., Aznar Cuadrado, R., Hirzberger, J., & Solanki, S. K. 2011, ApJ, 739, 92
Piskunov, N. & Valenti, J. A. 2017, A&A, 597, A16
Rempel, M. 2014, ApJ, 789, 132
Rosenthal, C. S., Bogdan, T. J., Carlsson, M., et al. 2002, ApJ, 564, 508
Scharmer, G. 2017, in SOLARNET IV: The Physics of the Sun from the Interior to the Outer Atmosphere, 85

Scharmer, G. B., Bjelksjo, K., Korhonen, T. K., Lindberg, B., & Petterson, B. 2003, in Proc. SPIE, Vol. 4853, Innovative Telescopes and Instrumentation for Solar Astrophysics, ed. S. L. Keil & S. V. Avakyan, 341–350
Scharmer, G. B., Narayan, G., Hillberg, T., et al. 2008, ApJ, 689, L69
Shetye, J., Verwichte, E., Stangalini, M., & Doyle, J. G. 2021, ApJ, 921, 30
Spruit, H. C. 1981, A&A, 98, 155
Srivastava, A. K., Ballester, J. L., Cally, P. S., et al. 2021, Journal of Geophysical Research (Space Physics), 126, e029097
Stangalini, M., Giannattasio, F., Erdélyi, R., et al. 2017, ApJ, 840, 19
Suematsu, Y., Ichimoto, K., Katsukawa, Y., et al. 2008, in Astronomical Society of the Pacific Conference Series, Vol. 397, First Results From Hinode, ed. S. A. Matthews, J. M. Davis, & L. K. Harra, 27
Uitenbroek, H. 2001, ApJ, 557, 389
van Doorsselaere, T., Verwichte, E., & Terradas, J. 2009, Space Sci. Rev., 149, 299
van Noort, M., Rouppe van der Voort, L., & Löfdahl, M. G. 2005, Sol. Phys., 228, 191
Vissers, G. & Rouppe van der Voort, L. 2012, ApJ, 750, 22
Wedemeyer, S., Freytag, B., Steffen, M., Ludwig, H. G., & Holweger, H. 2004, A&A, 414, 1121
Zaqarashvili, T. V. & Erdélyi, R. 2009, Space Sci. Rev., 149, 355
Zaqarashvili, T. V. & Skhirtladze, N. 2008, ApJ, 683, L91